



Study of Reynolds number effects on the aerodynamics of a moderately thick airfoil using a high-pressure wind tunnel

Claudia E. Brunner¹ · Janik Kiefer² · Martin O. L. Hansen² · Marcus Hultmark¹

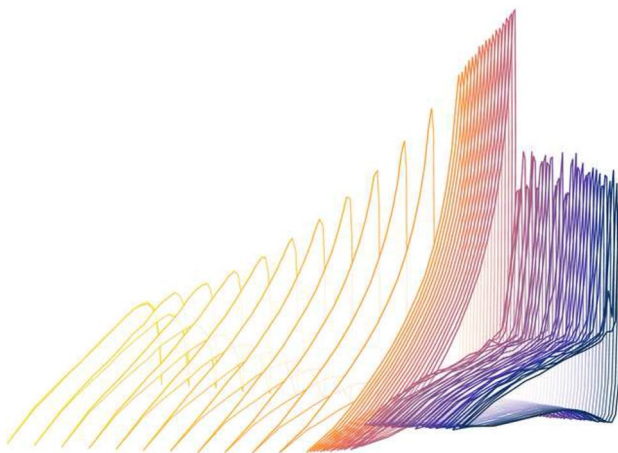
Received: 30 January 2021 / Revised: 15 July 2021 / Accepted: 15 July 2021

© The Author(s), under exclusive licence to Springer-Verlag GmbH Germany, part of Springer Nature 2021

Abstract

Reynolds number effects on the aerodynamics of the moderately thick NACA 0021 airfoil were experimentally studied by means of surface-pressure measurements. The use of a high-pressure wind tunnel allowed for variation of the chord Reynolds number over a range of $5.0 \times 10^5 \leq Re_c \leq 7.9 \times 10^6$. The angle of attack was incrementally increased and decreased over a range of $0^\circ \leq \alpha \leq 40^\circ$, spanning both the attached and stalled regime at all Reynolds numbers. As such, attached and separated conditions, as well as the static stall and reattachment processes were studied. A fundamental change in the flow behavior was observed around $Re_c = 2.0 \times 10^6$. As the Reynolds number increased beyond this value, the stall type gradually shifted from trailing-edge stall to leading-edge stall. The stall angle and the maximum lift coefficient increased with Reynolds number. Once the flow was separated, the separation point moved upstream, and the suction peak decreased in magnitude with increasing Reynolds number. Two distinct types of hysteresis in reattachment were observed. The data from this study are publicly available at <https://doi.org/10.34770/9mv0-zd78>.

Graphic abstract



1 Introduction

Accurately predicting the stall and post-stall behavior of an airfoil is crucial to many aerodynamic applications including wind turbines, fixed and rotary-wing aircraft, and compressors. However, predictions often remain challenging because neither theory nor numerical simulations accurately capture stall onset and separated-flow behavior of airfoils in high

✉ Claudia E. Brunner
cbrunner@princeton.edu

¹ Department of Mechanical and Aerospace Engineering, Princeton University, Princeton, New Jersey, USA

² Department of Wind Energy, Technical University of Denmark, Kgs. Lyngby, Denmark

Reynolds number flows. This study is concerned with such high Reynolds number flows.

Stall occurs when the viscous boundary layer on the suction side of the airfoil is unable to overcome the adverse pressure gradient of the flow behind the suction peak and separates from the airfoil surface. McCullough and Gault (1951) distinguish two types of stall behavior on airfoils: trailing-edge stall and leading-edge stall. Trailing-edge stall typically occurs when the boundary layer transitions to turbulence either upstream of the laminar separation point or via a laminar separation bubble, allowing the flow to stay attached beyond the laminar separation point. Separation of the turbulent boundary layer first occurs near the trailing edge, and the separation point gradually moves upstream with increasing angle of attack. Leading-edge stall typically occurs when the laminar boundary layer separates abruptly from the leading edge.

The location of the laminar to turbulence transition point along the airfoil surface depends strongly on the chord Reynolds number $Re_c = \rho U_\infty c \mu^{-1}$, where ρ is the flow density, U_∞ is the free-stream velocity, c is the chord length, and μ is the fluid viscosity. The higher Re_c , the further upstream the boundary layer transitions. Furthermore, the Reynolds number affects the velocity profile of the turbulent boundary layer. All else being equal, a higher Re_c leads to steeper velocity gradients near the airfoil surface. As a result, a turbulent boundary layer can withstand a greater adverse pressure gradient than a laminar one, but other Reynolds number effects are not fully understood.

Laminar separation bubbles play an important role in the above dynamics. They have been found to occur even at Reynolds numbers upward of $Re_c = 5.8 \times 10^6$ (McCullough and Gault 1951). However, they decrease in size with increasing Re_c , as the free shear layer transitions to turbulence earlier and thus reattaches closer to the initial separation point (Tani 1964). They have been found to act as trips on the airfoil surface, causing the boundary layer to transition to turbulence near the location of the laminar separation point (Mueller and Batill 1982). However, the reattached shear layer does not immediately exhibit the typical characteristics of a turbulent boundary layer. Instead, it retains higher Reynolds stresses, creating a steeper velocity profile and allowing the flow to stay attached longer than if it transitions to turbulence naturally (Schewe 2001).

An early study of Reynolds number effects on a wide range of airfoil sections showed a dependence of the maximum lift coefficient $C_{l,\max}$ on Reynolds number over the range of $4.1 \times 10^4 \leq Re_c \leq 3.1 \times 10^6$ (Jacobs and Sherman 1937). The thicker the airfoil, the more gradually $C_{l,\max}$ increased with Re_c . The state of the boundary layer is, however, also sensitive to surface roughness and other imperfections, as well as freestream turbulence, all of which can facilitate transition by introducing disturbances into the flow.

These early experiments suffered from several shortcomings, including particles in the airflow which roughened the leading edges, and high inflow turbulence in the wind tunnel, although the turbulence intensity was not quantified. These perturbations likely caused the boundary layer to become turbulent early on, even at relatively low Re_c , thus compounding effects of Reynolds number, freestream turbulence, and surface roughness. Similar experiments were conducted under somewhat improved conditions by Loftin and Bursnall (1948) who found that the only moderately thick airfoil tested experienced trailing-edge stall at all Re_c .

Disentangling the effects of Reynolds number, surface roughness, and freestream turbulence intensity and comparing the results of various studies on Reynolds number effects is challenging. Swalwell et al. (2001) studied the effects of turbulence intensity on a NACA 0021 airfoil at $Re_c = 3.5 \times 10^6$ and found that stall became more abrupt as freestream turbulence intensity decreased. At a turbulence intensity of 7%, gradual trailing edge stall was observed, while a turbulence intensity of 0.6% produced abrupt leading edge stall.

Achieving high Reynolds numbers in a controlled laboratory environment without experiencing disproportionate compressibility effects is challenging. Most facilities that operate in this range lack the ability to alter Re_c over a sufficient range to study trends in airfoil behavior with Reynolds number. Typically, such studies are performed in pressurized wind tunnels, in which Re_c can be varied by adjusting both the velocity and the density of the working fluid (Von Doenhoff and Abbott 1947, Schewe 2001, Wahls 2001, Hefer 2003). The present study examines Reynolds number effects on the aerodynamics of an airfoil of 21% thickness and an aspect ratio of 1.5 with naturally transitioning boundary layers. Attached and stalled conditions, as well as the stall and reattachment processes are elucidated. The tests are conducted in the High Reynolds number Test Facility (HRTF) at Princeton University, over a Reynolds number range of $5 \times 10^5 \leq Re_c \leq 7.9 \times 10^6$. Freestream turbulence and surface roughness are kept low in order to isolate Reynolds number effects. Data were acquired for a wide range of angles of attack, including angles well beyond the stall point. To the authors' knowledge, there are no existing data sets of a moderately thick symmetric airfoil that span a comparably large range of Re_c . It should be noted that this study does not represent a two-dimensional flow due to the low aspect ratio and associated three-dimensional effects, particularly in the separated region. As such, the data presented here serve as a qualitative indication of the effects of Reynolds number on airfoil aerodynamics.

2 Experimental setup

2.1 Wind tunnel

The airfoil tests were conducted in the High Reynolds number Test Facility (HRTF), a closed-loop wind tunnel that operates with dry air at internal static pressures up to 23.0 MPa. The gauge pressure during each individual test is given in Table 1. The density ρ of dry air changes almost linearly with increasing static pressure, while the dynamic viscosity μ is only a very weak function of pressure. This allows for high $Re_c = \rho U_\infty c \mu^{-1}$ at relatively low velocities U_∞ and reasonable chord lengths c . The use of high pressure has several advantages over atmospheric pressure. High Re_c can be achieved at low Mach numbers, avoiding compressibility effects. Furthermore, varying both velocity and pressure allows for a wider range of Re_c . Compared to other methods of achieving high Reynolds numbers, using pressurized air is one of the most cost- and energy-efficient methods.

The freestream velocity in the test section is measured 0.74 m upstream of the half-chord of the airfoil using a pitot-static tube and a differential pressure transducer (Validyne DP-15 with a range of 13.79 kPa). The exact velocities of each test are given in Table 1. The flow is conditioned using a coarse grid, a honeycomb grid, and a fine-mesh screen, followed by a short circular nozzle section with a contraction ratio of 2.5:1 upstream of the test section. This leads to a freestream turbulence intensity of $0.3\% \leq \sigma \leq 0.7\%$, where turbulence intensity increases with Re_c (Jiménez et al. 2010). The circular test section is 5.5-m-long with an inner diameter of $D = 0.49$ m. More information about the HRTF facility can be found in Miller et al. (2018) and Jiménez (2007).

The airfoil assembly is installed in an access port located 1.17-m-downstream of the entrance to the test section. The assembly, shown as a CAD rendering in Fig. 1a, consists of the airfoil with two endplates, a mounting rod, a rotary table, and a load cell. The load cell was not used in the current study. Instead, forces and moments were obtained by integrating the pressure distribution. A rotary table equipped with a stepper motor, and a CUI AMT103 capacitive encoder is used to measure and alter the angle of attack. The rotary table and stepper motor are coupled through a worm gear, which prevents the angle of attack from being changed by aerodynamic moments through self-retention of the gear. Microstepping and gear reduction allow the angle to be adjusted in 0.075° increments, while the encoder has an angle resolution of 0.176° . The rotation axis of the airfoil is at the half-chord.

2.2 Airfoil

Many studies related to the performance of lift-based vertical-axis wind turbines use a symmetric NACA 4-series airfoil section with moderate thickness, e.g., Raciti Castelli et al. (2011), Miller et al. (2018), and FloWind (1996). A NACA 0021 airfoil was therefore chosen for this study to provide an experimental benchmark across a wide range of Reynolds numbers and angles of attack. The model has a chord length of $c = 0.17$ m, which yields a trailing-edge thickness of 0.748 mm. This allows for the installation of a pressure tap at the trailing edge. The airfoil and all of its components are shown in an exploded view in Fig. 2.

Due to the circular cross-section of the HRTF, the airfoil cannot span the full width of the test section. In order to ensure that the airfoil could undergo a full rotation inside the tunnel, the aspect ratio was limited to 1.5. However, this is expected to introduce three-dimensional effects due to tip vortices, particularly in the separated flow post-stall. The

Table 1 Individual experimental runs in the pressurized High Reynolds number Test Facility at Princeton University

Re_c (–)	P (MPa)	ρ (kg/m ³)	U_∞ (m/s)	Number of angles	Sample time per angle (s)	$\Delta\alpha$ (°)	$\Delta\alpha$ around stall (°)
0.5×10^6	0.80	9.5	5.96	55	120	5	0.50
1.0×10^6	1.50	17.6	6.37	49	120	5	0.50
1.5×10^6	2.20	26.1	6.39	27	60	5	1.00
2.0×10^6	4.19	49.7	4.51	63	40	2	0.25
3.0×10^6	12.55	146.6	2.54	63	40	2	0.25
4.0×10^6	12.48	145.5	3.41	63	40	2	0.25
5.0×10^6	12.51	144.5	4.30	63	40	2	0.25
5.9×10^6	21.80	239.6	3.55	63	40	2	0.25
7.0×10^6	23.00	246.7	4.13	63	30	2	0.25
7.9×10^6	22.85	249.2	4.64	63	30	2	0.25

$\Delta\alpha$ denotes the angle resolution

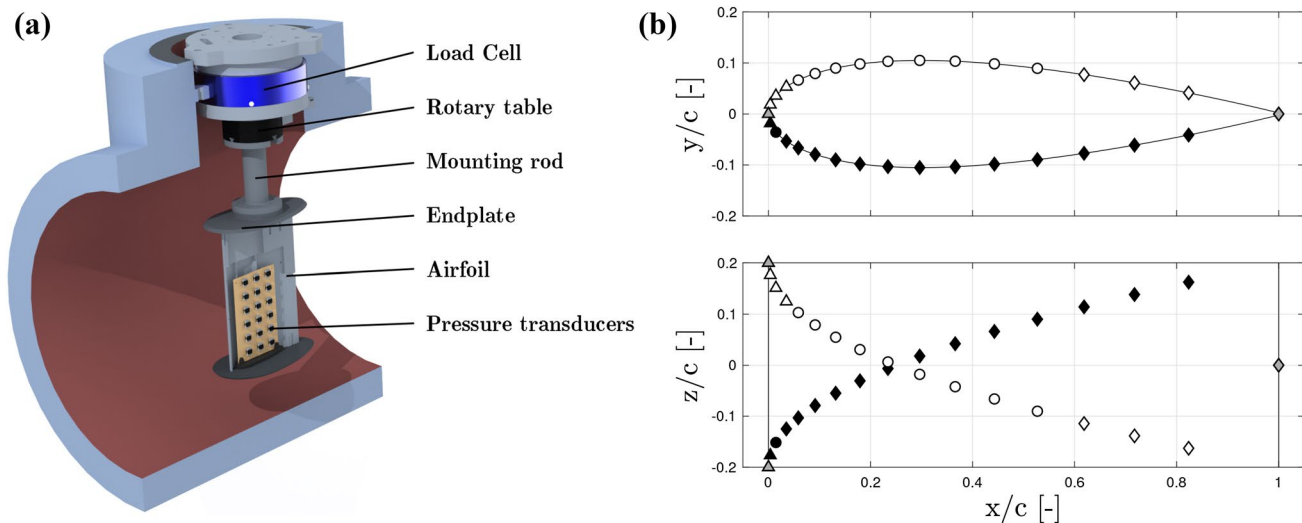


Fig. 1 **a** Cutaway CAD rendering of the test section revealing the airfoil model and measurement assembly. Flow goes from left to right. **b** Tap locations on the NACA0021 profile used in the experiment. Sensing ranges of the pressure transducers: $\triangle = \pm 10$ kPa, $\circ = \pm$

6.9 kPa, $\diamond = \pm 2.5$ kPa. White markers indicate suction-side taps, black markers indicate pressure-side taps, and grey markers indicate leading-edge and trailing-edge taps

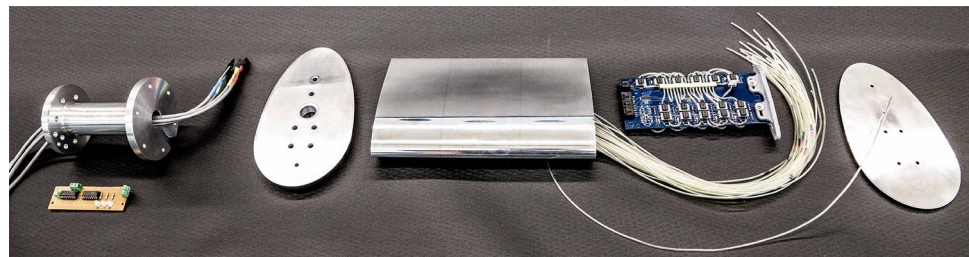


Fig. 2 Exploded view of the airfoil assembly. From left to right: mounting rod with electric wiring and binary counter for hardware-timed multiplexer control, upper endplate, polished airfoil with 33

embedded pressure taps and corresponding pressure tubing, PCB board including multiplexers and pressure sensors, and lower endplate

airfoil is equipped with endplates, which somewhat alleviate this issue by increasing the effective aspect ratio (cf. Sect. 4). However, studies on circular cylinders have shown that the use of endplates at low aspect ratios leads to three-dimensional effects on the shedding behavior (Fox and West 1990; Szepessy and Bearman 1992). As such, the flow field is expected to remain three-dimensional, and the applicability of the observed phenomena to two-dimensional flows remains to be verified. Spatial limitations of the access-port used to install the airfoil assembly make circular endplates unfeasible. Instead, the shape of the endplates is composed of two half-ellipses, one encompassing the leading edge of the airfoil and the other the trailing edge. The centerpoints of both half-ellipses are located on the centerline of the airfoil at $x/c = 0.3$, the point of maximum thickness.

Equation 1 describes the shape of the endplates. The coefficient for the semi-major axis of the leading edge half-ellipse is $a_l = -76/170$ and that of the trailing edge

half-ellipse is $a_t = 144/170$. For both half-ellipses, the coefficient of the semi-minor axis is $b = 6/17$, which results in a tangential transition between the two.

$$y(x) = \begin{cases} \pm b \sqrt{1 - \frac{x^2}{a_l^2}}, & x \in [a_l, 0] \\ \pm b \sqrt{1 - \frac{x^2}{a_t^2}}, & x \in [0, a_t] \end{cases} \quad (1)$$

The airfoil and endplates are made of high-strength aluminum. The airfoil is hollow, and the air inside it equilibrates to the static tunnel pressure. The minimum wall thickness of the airfoil is 2 mm, and the support structure is considerably thicker, preventing deformation due to the extreme operating conditions.

The surfaces were sanded using sandpaper of decreasing grain size, and finally polished to a mirror surface finish using polishing fluid (cf. Fig. 2). Select surface areas were

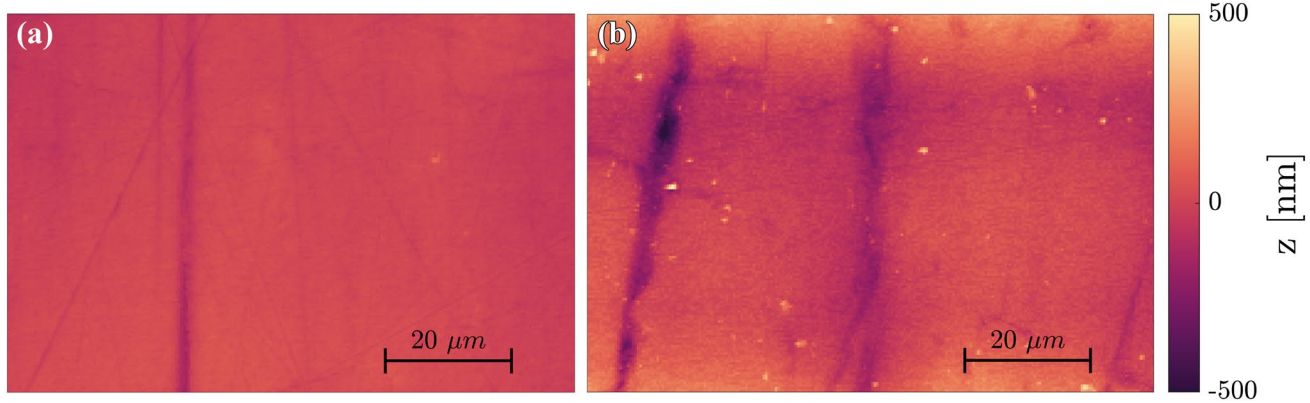


Fig. 3 Atomic force microscopy of the airfoil's pressure side **a** and suction side **b** was performed on a Bruker NanoMan microscope using an RTESPA-300 tip with nominal tip radius 8 nm, spring constant 40 N/m, and resonance frequency 300 kHz

examined using atomic force microscopy. Figure 3 shows samples of both sides of the airfoil. Ridges caused by sanding are visible in the images. Due to manual polishing, the suction side had a slightly higher roughness length compared to the pressure side. The root mean square of the surface roughness was measured to be 90 nm on the suction side and 30 nm on the pressure side. In viscous units, this corresponds to approximately $k^+ \leq 0.2$ on the suction side for $x \geq 0.05$ at all Re_c , which is well within the viscous sublayer and can thus be considered aerodynamically smooth.

2.3 Surface pressure sensing

Airfoil surface pressures are acquired using 32 pressure taps. Each individual pressure tap consists of a brass insert of 3-mm-diameter, which was press-fit into the aluminum body of the airfoil. A 0.5-mm-diameter hole was drilled into the brass insert, which serves as the sensing hole for the pressure at the airfoil surface. The height difference between the airfoil surface and the brass inserts containing the pressure taps is $\sim 1 \mu\text{m}$, which corresponds to approximately $\Delta y^+ \leq 2.2$ for all Re_c . A small cavity is present around each brass insert, with a width of $\sim 50 \mu\text{m}$ and a depth of $\sim 20 \mu\text{m}$. According to Holmes et al. (1986), the critical Reynolds number based on the gap height or width h , above which a gap induces premature transition is $Re_{h, crit} = 15000$. Even at the highest Re_c studied here, the gap width of $h \sim 50 \mu\text{m}$ yields $Re_h \sim 2300$. Thus, the cavities are not expected to induce premature transition.

The layout of the pressure taps along with their sensor ranges is shown in Fig. 1b. The chordwise and spanwise locations of the pressure taps in non-dimensional coordinates can be determined using Eqs. 2a and 2b, respectively. The equations yield the location of each tap $j \in \{1, 2, \dots, n\}$, where n is the number of taps per surface. In this study, $n = 17$.

$$x_j = \begin{cases} \xi \left(\frac{j-1}{n-1} \right)^2, & j \in \{1, 2, \dots, n-1\} \\ 1, & j = n \end{cases} \quad (2a)$$

$$z_j = \begin{cases} 0.4 \sqrt{\xi} \frac{j-1}{n-1} - 0.2, & j \in \{1, 2, \dots, n-1\} \\ 0, & j = n \end{cases} \quad (2b)$$

The chordwise distribution concentrates the pressure taps near the leading edge, where higher pressure gradients are expected due to the increased surface curvature. For $j = 1$, the equations yield a chordwise location of $x_1 = 0$, and for $j = n$ they yield $x_n = 1$. Thus, the first tap is located at the leading edge, and the last tap at the trailing edge at mid-span, parallel to the centerline of the airfoil. The scaling parameter ξ is then used to condense the distribution forward such that the second-to-last tap is located a distance $1 - \xi$ away from the trailing edge. The airfoil must be thick enough to accommodate the brass-insert and tubing that connect the tap to the pressure transducer inside the airfoil. In this study $\xi = 14/17$, which for the given chord length of 170 mm places the second-to-last tap 30 mm away from the trailing edge.

The spanwise distribution reduces not only the potential interference of neighboring taps due to flow disturbances caused by the sensing holes, but also obstructions of the brass inserts and tubing inside the airfoil. Two pressure taps are located at the leading edge, but only one was used for measurements.

Each tap is connected to a temperature-compensated Honeywell TruStability HSC differential pressure transducer using $\leq 250 \text{ mm}$ long urethane tubing with 1.6-mm-diameter. All of the pressure transducers are located inside the airfoil in order to minimize tube lengths. As shown in Fig. 1b, three transducer sensing ranges are used: $\pm 10 \text{ kPa}$ for the highest anticipated pressure ranges, $\pm 6.9 \text{ kPa}$ for intermediate ranges, and $\pm 2.5 \text{ kPa}$ for the lowest ranges.

A pitot-static probe located 0.38-m-upstream of the airfoil half-chord provides a static reference pressure for the differential pressure transducers. The transducers are mounted on a custom-made PCB-board. Four embedded ADG608 8-channel multiplexers are used to scan through the 32 pressure taps. Two SN7474 dual flip-flops function as a 3-bit binary counter to achieve hardware-timed triggering of the multiplexers.

The system described above not only cost significantly less than comparable commercially available pressure scanners, but also provided better resolution across the airfoil surface due to the different ranges of the individual pressure transducers. So far, the system has withstood more than 800 hours of operation inside the high-pressure, high-oxygen environment of the wind tunnel without signs of degradation.

3 Experimental procedure

The Reynolds number for each experimental run is set by choosing an appropriate combination of free-stream velocity and static pressure (i.e., density). Free-stream velocities tested are in the range of $2.5 \text{ m/s} \leq U_{\infty} \leq 6.4 \text{ m/s}$, leading to free-stream turbulence intensities of $0.3\% \leq \sigma \leq 0.7\%$ (Jiménez et al. 2010). The pressures are $0.8 \text{ MPa} \leq p_{\infty} \leq 23.0 \text{ MPa}$, as shown in Table 1. Since these two parameters can be adjusted independently of each other in this experimental setup, different combinations can yield the same Re_c but different magnitudes of the aerodynamic forces. This is because the forces scale linearly with density but quadratically with velocity. Thus, for a given Re_c , a high velocity and low pressure will lead to larger forces than vice versa. Given the limited sensing ranges of the pressure transducers, this is exploited to achieve measurable forces at all Re_c . Lower Re_c are achieved using lower pressures and higher velocities to achieve maximum sensor loading and thus better measurement accuracy, whereas data at higher Re_c are obtained at maximum tunnel pressure and lowest possible velocities to avoid exceeding the sensing ranges of the pressure transducers. Nevertheless, for $Re_c \geq 7.0 \times 10^6$ the sensing ranges of some of the pressure transducers near the leading edge are exceeded at the angles prior to stall. These data points, and any parameter that is a function of them, are omitted. The use of very high pressures at high Re_c further ensured that the forces acting on the airfoil model never exceeded 215 N, so as to protect the airfoil and supporting rod from deformations.

For each test case, the angle of attack is incrementally increased from $\alpha = -10^\circ$ to $\alpha = 40^\circ$ and then decreased back to $\alpha = -10^\circ$. The region around the stall angle is sampled at smaller angle increments to precisely capture the stall angle and development. The stall angle α_{stall} is here defined as the

angle which produces the highest lift coefficient $C_{l,max}$ while the angle of attack is incrementally increased from $\alpha = 0^\circ$ to $\alpha = 40^\circ$. The angle resolution for every run is given in Table 1. Comparison tests are conducted to assure that the measurements at positive and negative α are identical.

Fully automated control of the experiment as well as data acquisition is realized in Labview. The acquisition frequency is 10 kHz, and the scanning frequency of the surface pressure transducers is 2 Hz. The sampling time necessary to achieve converging results at a given angle increases with decreasing velocity due to lower sensor loading.

The real-gas effects experienced here are small and are accounted for using a relationship detailed in Zagarola (1996). The density and viscosity at each data point are calculated from static pressure and temperature measurements by employing this real-gas relationship. All data are time-averaged for each angle during post-processing. Parameters are given in Table 1. For error analysis, see appendix.

4 Corrections

In order to compare the data to existing NACA 0021 experimental data, as well as to provide an equivalent two-dimensional dataset for use in models and simulations, several corrections were applied. However, the experimental results, and their discussion presented herein are based entirely on uncorrected data unless otherwise stated.

The first correction addresses the blockage in the wind tunnel due to the airfoil and mounting structure. Traditional blockage corrections for airfoils spanning the entire width of a rectangular tunnel could not be applied due to the circular cross-section of the HRTF. Instead, the velocity was corrected according to Eq. 3 using the ratio of the maximum cross-sectional area of the airfoil and mounting apparatus A_m , which lay at the rotation axis, and the total cross-sectional area of the test section A_t . A_m increases with α .

$$u_e = \frac{u}{1 - \frac{A_m}{A_t}}, \quad (3)$$

The two remaining corrections address the presence of tip vortices and downwash. As such, they are deemed to have no physical basis in separated flow. Therefore, the corrections are applied only throughout the attached-flow region, resulting in lower stall angles compared to the uncorrected data. The difference between the corrected and uncorrected stall angles is then applied as an offset to all separated flow data in order to create a continuous lift curve. The first of these two corrections accounts for the endplates, which lead to a larger effective aspect ratio due to attenuation of tip vortices. Here, the correction method described in Hoerner

(1975) is used, which models the endplate-corrected aspect ratio AR_p as

$$AR_p = AR_g + \frac{kh}{b}, \quad (4)$$

where AR_g is the geometric aspect ratio, h is the endplate height measured from the center line, b is the airfoil span, and k is a scaling factor. As suggested by Hoerner (1975), we use $k = 1.9$, which gives a corrected aspect ratio of $AR_p = 2.39$. This aspect ratio AR_p is then used to determine the effective aspect ratio AR_e which is needed to reduce the lift and drag coefficients to equivalent two-dimensional values.

The method described in Jacobs and Anderson (1931) is used for the last correction. First, the effective ratio AR_e is computed using the endplate-corrected aspect ratio AR_p , the effective span b_e , and the test section diameter D , as shown in Eq. 5.

$$AR_e = \frac{AR_p}{1 - \frac{1}{2} \left(\frac{b_e}{D} \right)^2} \quad (5)$$

This effective aspect ratio AR_e is then used to assign each lift coefficient C_l to a new angle of attack α' as shown in Eq. 6.

$$\alpha' = \alpha - \frac{180}{\pi^2} \frac{C_l}{AR_e} (1 + \tau) \quad (6)$$

Finally, each lift coefficient is assigned a new drag coefficient C'_d as shown in Eq. 7.

$$C'_d = C_d - \frac{C_l^2}{\pi AR_e} (1 + \sigma) \quad (7)$$

The factors τ and σ account for the change in elliptical span loading along the rectangular planform of the airfoil. Jacobs and Anderson (1931) provide a graph of τ and σ as functions of aspect ratio. Extrapolation of the graph to $AR_p = 2.39$ yielded $\tau = 0.096$ and $\sigma = 0.091$. Despite the high Re_c achieved in the pressurized wind tunnel, the free-stream velocities remain below 10 m/s. Since the speed of sound is a very weak function of pressure, the Mach numbers are $M \leq 0.03$. Thus, no Mach number corrections were applied. Corrected data from the present study are shown in Fig. 4 along with several existing datasets. Unless otherwise noted, all data presented in the results section below are uncorrected.

5 Results

5.1 Validation

When corrected for blockage and aspect ratio (cf. Sect. 4), the current data show good agreement with existing NACA 0021 datasets in the lift coefficient throughout the attached region. Figure 4a shows the uncorrected and corrected lift coefficients from the current study at $Re_c = 2.0 \times 10^6$ along with a data set taken from Angell et al. (1990) at $Re_c = 1.9 \times 10^6$. The model in this study had an aspect ratio of $AR = 2.9$. The agreement in the attached region is reasonably good, but the stall is somewhat more abrupt in the current study.

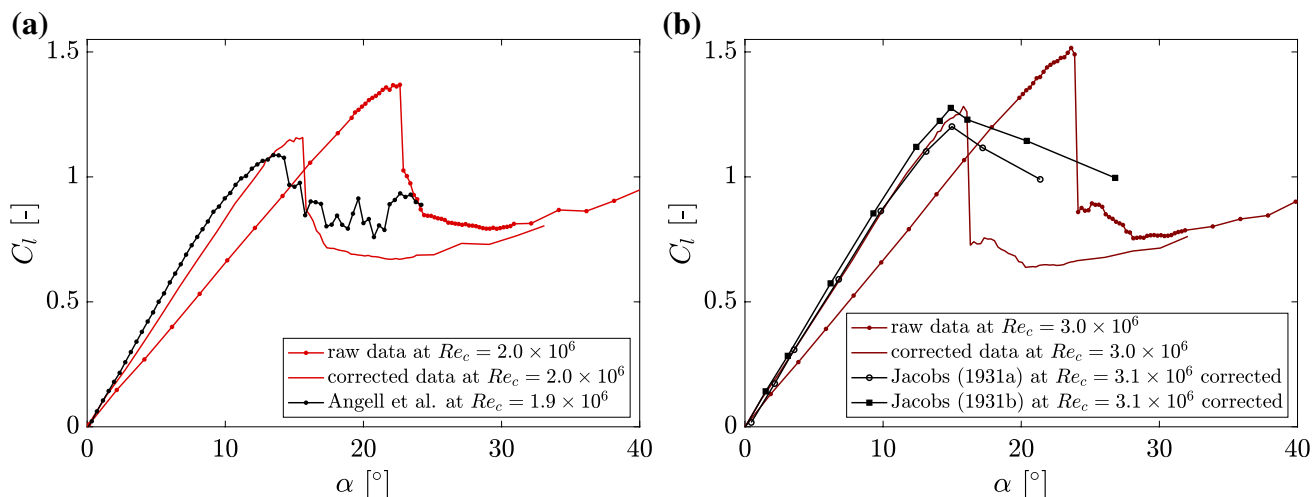


Fig. 4 **a** Corrected data at $Re_c = 2.0 \times 10^6$ in comparison with data from Angell et al. (1990). **b** Raw lift data at $Re_c = 3.0 \times 10^6$ in comparison with corrected data and data from NACA reports TN-385 (Jacobs 1931b) and TR-391 (Jacobs 1931a)

Similarly, Fig. 4b shows uncorrected and corrected lift coefficient measurements at $Re_c = 3.0 \times 10^6$, together with two early datasets of a NACA 0021 airfoil at $Re_c = 3.1 \times 10^6$ taken from Jacobs (1931b) and Jacobs (1931a). The corrected data from the present study agree well with the previous (corrected) data throughout the attached region. However, while the data from this study show drastic leading-edge stall, the previous data sets indicate more gradual stall development. In contrast to the data presented here, both of the datasets from Jacobs were obtained under relatively high levels of freestream turbulence. Because the following discussion is largely qualitative and not necessarily representative of a two-dimensional airfoil, all data presented below are uncorrected.

5.2 Attached flow

Minor Reynolds number effects are present in the attached flow region. Short laminar separation bubbles are visible in the pressure distributions for $Re_c \leq 2.0 \times 10^6$. For $Re_c \geq 3.0 \times 10^6$, the spatial resolution of the pressure sensors is too low to determine whether a laminar separation

bubble is present or the flow transitions to turbulence naturally ahead of the hypothetical laminar separation point, as the bubble size is expected to decrease with increasing Re_c . The pressure at the suction peak $C_{p,min}$ decreases slightly with increasing Re_c (cf. Fig. 5a).

Figure 5b shows the lift coefficient C_l as a function of angle of attack α . The linear region extends to at least $\alpha = 15^\circ$ for all Re_c . Figure 7a shows the pressure drag coefficient C_d as a function of α . For the Reynolds numbers considered here, the drag due to skin friction was determined to be negligible. However, the limited spatial resolution of the pressure taps might introduce a bias in the drag coefficient measurements. For $Re_c \leq 1.5 \times 10^6$, C_d decreases with increasing Re_c throughout the fully-attached region, while for $Re_c \geq 1.5 \times 10^6$ no Reynolds number effects are visible. This trend is mirrored in the minimum drag coefficient $C_{d,min}$, measured at $\alpha = 0^\circ$ (cf. Fig. 6a).

The aerodynamic center *a.c.* lies slightly upstream of the quarter chord point for all Re_c measured. It moves upstream with increasing Reynolds number for $Re_c \leq 1.5 \times 10^6$ before moving steadily downstream for $Re_c \geq 1.5 \times 10^6$ (cf. Fig. 6b). As a result, the moment around the quarter chord

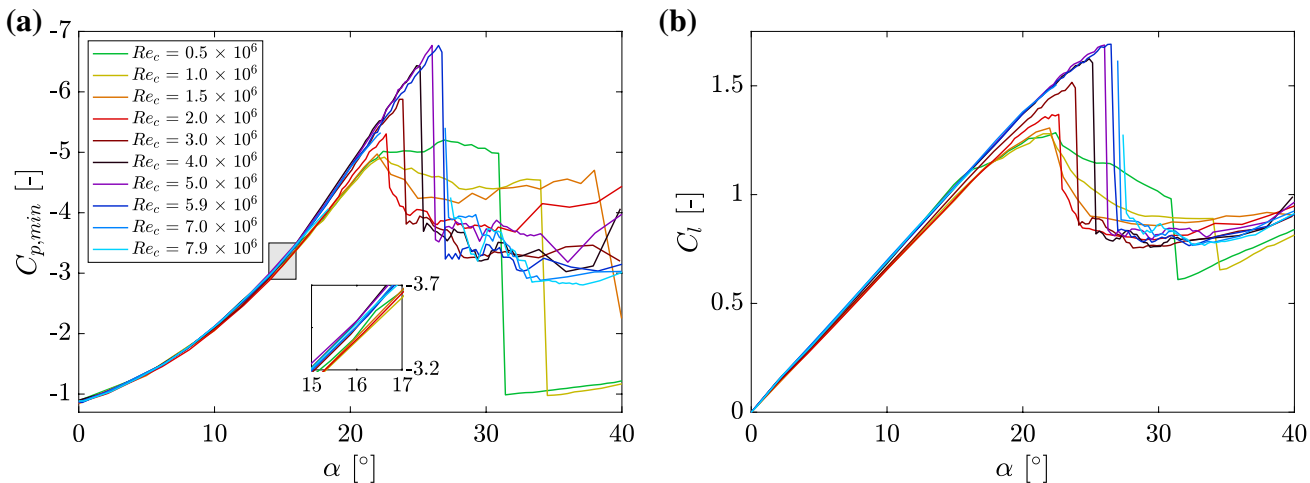


Fig. 5 **a** The minimum pressure coefficient $C_{p,min}$ along the airfoil surface, also known as the suction peak. **b** Uncorrected lift coefficient C_l . Data points at which pressures exceeded transducer sensing ranges were omitted. The legend applies to both plots

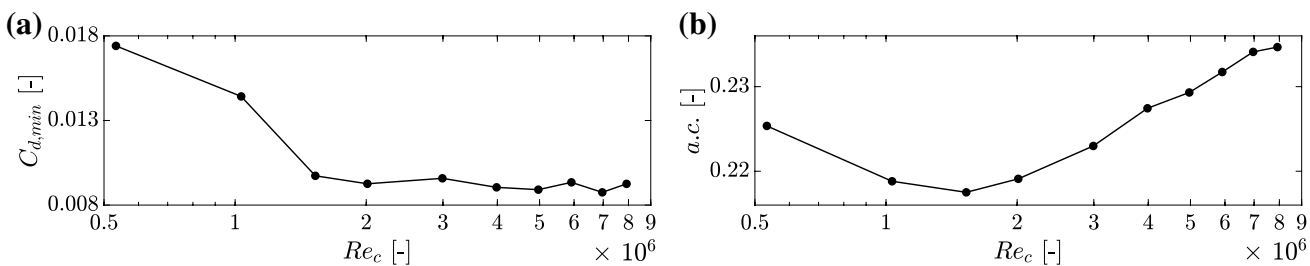


Fig. 6 **a** Minimum drag coefficient, recorded at $\alpha = 0^\circ$. **b** Mean aerodynamic center over $0^\circ \leq \alpha \leq 15^\circ$

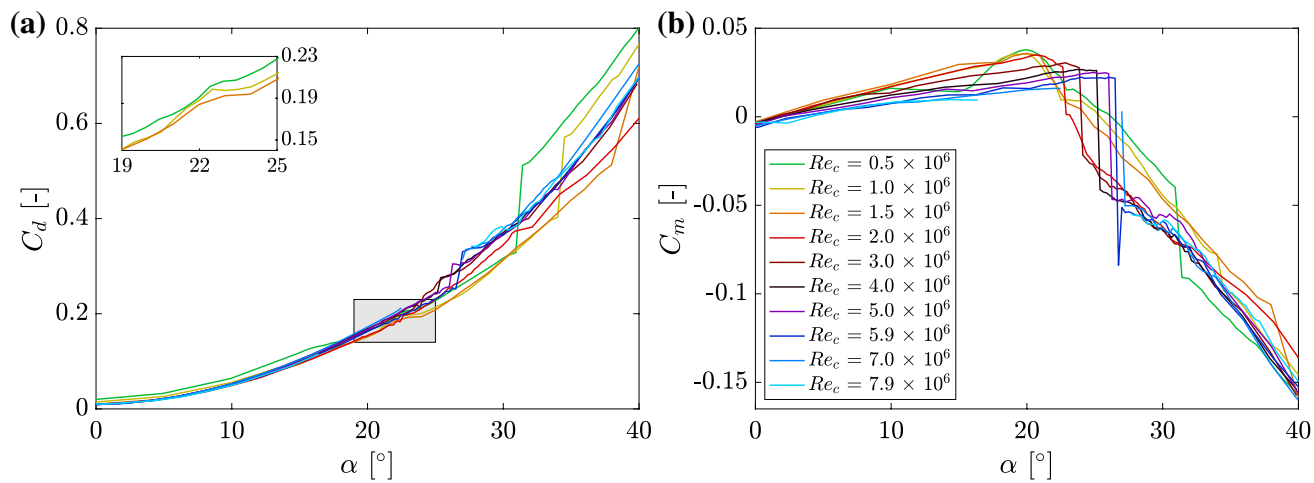


Fig. 7 **a** Drag coefficient C_d . All data were acquired by integrating the surface pressure distribution. The subplot highlights the region around stall for the lowest Reynolds numbers. **b** The moment coefficient

around the quarter chord. In both plots data points were omitted at which pressures exceeded transducer sensing ranges. The legend applies to both plots

$C_{m,\frac{c}{4}}$ increases slightly with α at all Reynolds numbers (cf. Fig. 7b). For all angles up to the stall angle, $C_{m,\frac{c}{4}}$ remains positive, indicating a nose-up moment as per convention.

5.3 Stall

Three distinct types of flow separation are observed. Leading-edge stall is taken to mean separation that is first observed within approximately $0.2c$ of the leading edge, while trailing-edge stall is taken to mean any separation that is first observed downstream of $0.2c$. As the following discussion reveals, these differentiations are somewhat arbitrary because the location of initial separation cannot always be

determined exactly. Separation that occurs within $0.01c$ is referred to as immediate-leading-edge stall.

The stall behavior varies with Re_c , with trailing-edge stall present at the lower Re_c , leading-edge stall at the higher Re_c , and an intermediate Reynolds number region displaying both. The angle at which trailing-edge separation first occurs increases with Re_c . However, the exact angle of separation onset cannot be determined due to the scarcity of pressure taps near the trailing edge. For $Re_c \leq 1.5 \times 10^6$, the flow begins to separate gradually from the trailing edge even while the magnitude of the suction peak and the lift coefficient continue to increase. This results in a rounded lift curve and a gradual decrease in lift after α_{stall} is surpassed (cf. Fig. 5b).

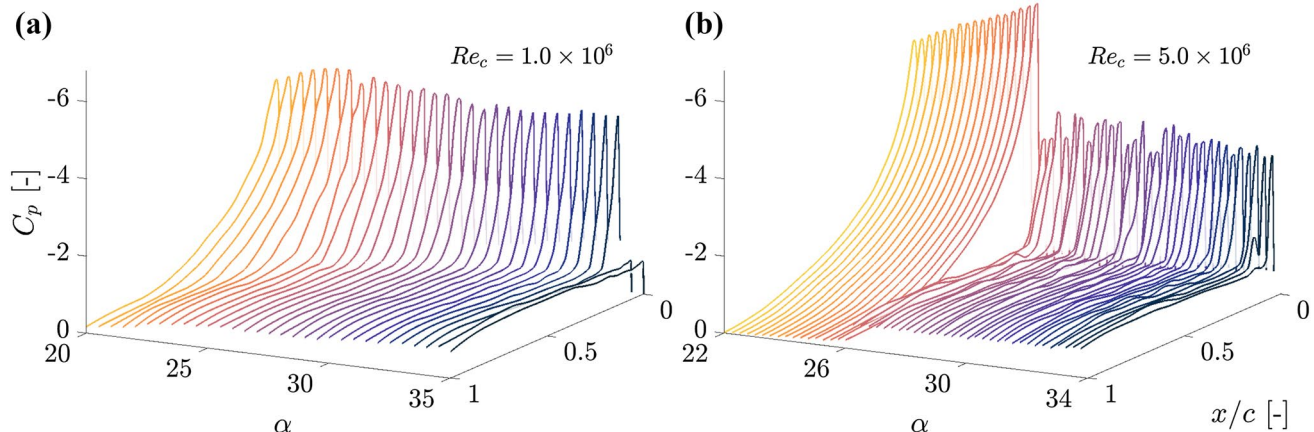


Fig. 8 Time-averaged pressure distributions in the stalled region at Reynolds numbers $Re_c = 1.0 \times 10^6$ **a** and $Re_c = 5.0 \times 10^6$ **b** over a wide range of angles of attack in increments of 0.5° and 0.25° , respectively

For $2.0 \times 10^6 \leq Re_c \leq 3.0 \times 10^6$, trailing-edge separation is visible at angles immediately below α_{stall} , resulting in a flattening of the lift curve prior to a sudden drop in C_l induced by leading-edge stall (cf. Fig. 5b). At $Re_c \geq 4.0 \times 10^6$, no trailing-edge stall is visible. Instead, the airfoil stalls abruptly from the leading edge (cf. Fig. 8b). This leading-edge stall for $Re_c \geq 2.0 \times 10^6$ causes a significant drop in the magnitude of the suction peak. Once leading-edge stall has occurred, the separation point is almost invariant with Re_c , suggesting that separation might be laminar.

Both α_{stall} and $C_{l,max}$ are almost constant for $Re_c \leq 1.5 \times 10^6$ and increase with Reynolds number for $Re_c \geq 2.0 \times 10^6$, leveling off slightly at the highest Re_c (cf. Fig. 9). The drag coefficient C_d exhibits a slight bump around the stall angle for $Re_c \leq 1.5 \times 10^6$ (cf. inserted plot in Fig. 7a). At $Re_c = 2.0 \times 10^6$, the stall onset has no visible signature in C_d despite the abrupt loss of lift. For $Re_c \geq 3.0 \times 10^6$, a sudden increase in C_d occurs at α_{stall} , the magnitude of which increases with Re_c . As a result, the lower Re_c , which produced higher drag while the flow was

attached, produce lower drag once the airfoil is stalled. The moment coefficient $C_{m,\frac{c}{4}}$ reaches its maximum value at α_{stall} (cf. Fig. 7b). Similarly to C_l , it decreases gradually for $Re_c \leq 1.5 \times 10^6$ and abruptly for $Re_c \geq 2.0 \times 10^6$ as α surpasses the stall angle, quickly becoming negative for all Re_c and thus causing a nose-down moment.

5.4 Separated flow

The stalled-flow pressure distributions and all associated quantities showed significantly larger fluctuations compared to the pressure distributions in attached flows, presumably due to shedding or turbulence in the separated region. Data were smoothed for clarity using a moving average.

The separation behavior at the lower Re_c exhibits two noteworthy features. Figure 10a shows the pressure distributions along the suction side at $\alpha = 24.25^\circ$ for various Re_c . At this angle, the flows for $Re_c \geq 4.0 \times 10^6$ are still fully attached, whereas the flows for $Re_c \leq 3.0 \times 10^6$ separate between $0.16c$ and $0.30c$. Interestingly, the location of

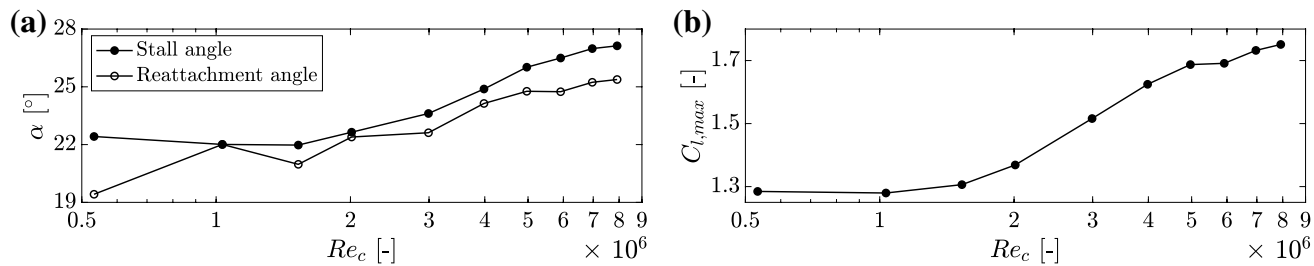


Fig. 9 **a** Stall angle α_{stall} , defined as the angle at which $C_{l,max}$ occurs, and reattachment angle. **b** Maximum lift coefficient $C_{l,max}$

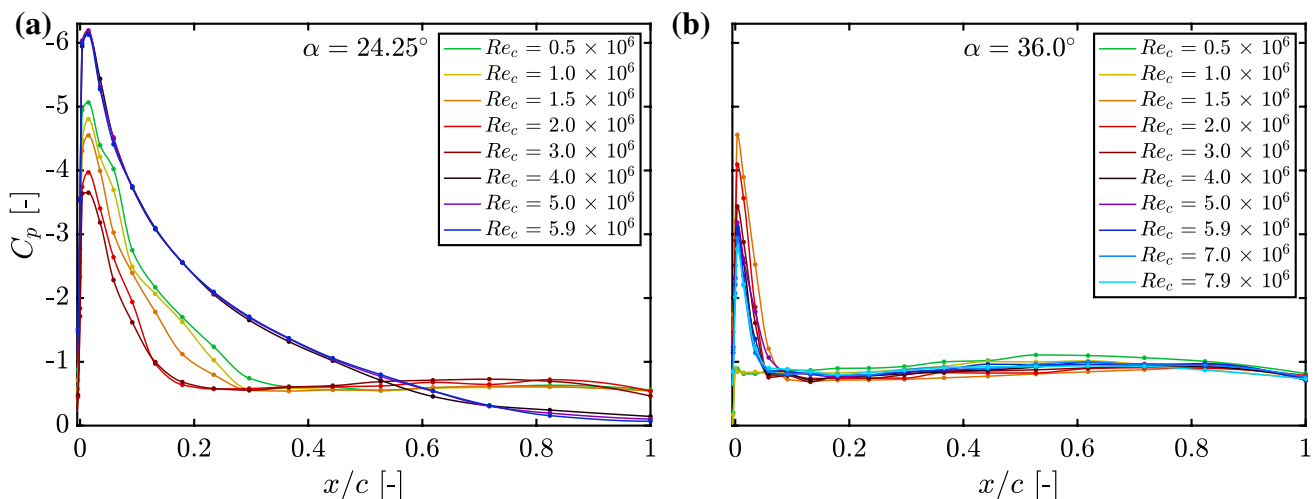


Fig. 10 Time-averaged pressure distributions at various Reynolds numbers along the suction side of the airfoil for angles of attack of $\alpha = 24.25^\circ$ **a** and $\alpha = 36.0^\circ$ **b**

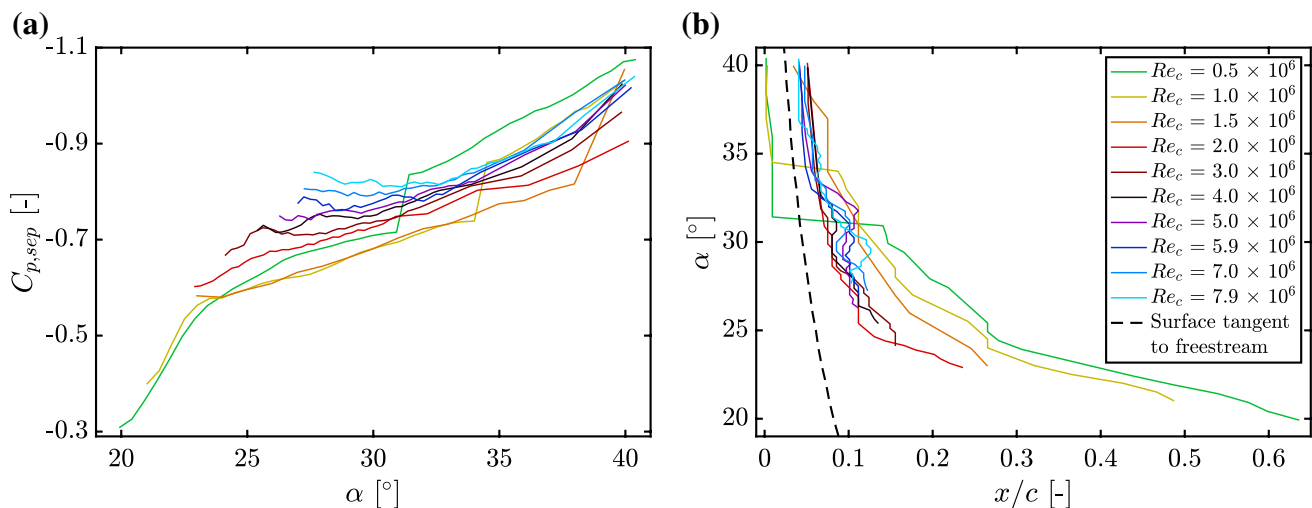


Fig. 11 **a** Mean pressure coefficient along the surface downstream of the separation point, referred to as $C_{p,sep}$. **b** Chord position at which separation occurs. The separation points were determined by visual inspection of the pressure distributions. Data were smoothed using a

moving average due to the discrete number of pressure sensors. The dotted line indicates the chord position at which the airfoil surface is tangent to the freestream

the separation point moves upstream with increasing Re_c , while $C_{p,min}$ decreases. Figure 11b reveals that this trend in the location of the separation point holds true over a wide range of angles from the onset of separation until at least $\alpha = 31^\circ$. For $Re_c \geq 3.0 \times 10^6$, the separation point appears within $0.2c$ of the leading edge and is Reynolds number invariant (cf. Fig. 10b).

As α is increased far beyond α_{stall} , the separation points for $Re_c \leq 1.5 \times 10^6$, which up until then were located at least $0.1c$ downstream of the leading edge, experience a significant shift forward to approximately $0.01c$ (cf. Figs. 8a and 11b). They thus move from a location just behind the point at which the airfoil surface is tangent to the flow to a location directly at the leading edge. This shift occurs at $\alpha = 30.9^\circ$ for $Re_c = 0.5 \times 10^6$ and at $\alpha = 34.0^\circ$ for $Re_c = 1.0 \times 10^6$. An equivalent shift, though less obvious in the data, occurs within $38.0^\circ \leq \alpha \leq 40.0^\circ$ for $Re_c = 1.5 \times 10^6$. This condition is distinct from the leading-edge stall otherwise observed in these data due to the complete absence of a suction peak and is thus referred to as immediate-leading-edge stall.

The relationship between the separation point and the suction peak changes with Reynolds number. At $Re_c \leq 1.5 \times 10^6$, trailing-edge stall does not lead to a significant decrease in the magnitude of the suction peak. Instead, the separation point moves gradually forward with increasing α , creating an ever steeper pressure gradient between the suction peak and the separated region until the separation point jumps forward (cf. Fig. 8a). When this happens, the suction peak disappears and the pressure becomes relatively constant along the entire suction side. For $Re_c \geq 2.0 \times 10^6$, the post-stall suction peak similarly has almost no dependence on α , but the separation point

moves only slightly upstream as α is increased and appears to approach a location approximately $0.05c$ downstream of the leading edge, as shown for $Re_c = 5.0 \times 10^6$ in Fig. 8b.

The mean surface pressure downstream of the separation point $C_{p,sep}$ (cf. Fig. 11a), provides insight into the pressure field. The pressure decreases with increasing Re_c across the entire range of Reynolds numbers, except for the cases where the separation point has shifted to $0.01c$. Where the separation point shifts upstream, the pressure decreases abruptly to values comparable to those at the highest Reynolds numbers tested. The shift in separation point also results in a decrease in pressure on the bottom side of the airfoil, while the stagnation point moves slightly upstream. The pressure at the trailing edge is unchanged.

The Reynolds number trends in the pressure distribution are visible in the force and moment coefficients. At angles above α_{stall} , C_l decreases with increasing Reynolds number for $Re_c \leq 1.5 \times 10^6$ (cf. Fig. 5b). However, when the separation point jumps to $0.01c$, there is a sudden drop in C_l . Immediately following stall, the drag coefficient C_d exhibits a slight Reynolds number dependence, but as α is increased further, the drag coefficients collapse onto a single curve for $Re_c \geq 3.0 \times 10^6$. For $Re_c \leq 2.0 \times 10^6$, C_d is slightly lower until the separation point shifts forward. The shift causes C_d to increase drastically, presumably due to the increased size of the wake. The moment coefficient $C_{m,\frac{c}{4}}$ decreases with increasing Reynolds number for $Re_c \leq 1.5 \times 10^6$ before the separation point jumps to $0.01c$. The jump results in a drop in $C_{m,\frac{c}{4}}$, thus increasing the nose-down moment. For $Re_c \geq 2.0 \times 10^6$, the $C_{m,\frac{c}{4}}$ for all

Re_c collapse well onto a single curve with a steep negative slope indicating an increasingly drastic nose-down moment.

5.5 Hysteresis in angle of attack

As the angle of attack is incrementally decreased from $\alpha = 40^\circ$ to $\alpha = 0^\circ$, no notable hysteresis is found within the stalled region or the fully attached region. However, two distinct types of hysteresis are observed in the reattachment of the flow, one for $Re_c \leq 1.5 \times 10^6$ and the other for $Re_c \geq 3.0 \times 10^6$. The reattachment angle is found to be more volatile than the stall angle, likely due to the high levels of turbulence and shedding in the separated region, and associated instantaneous fluctuations in the pressure distribution. As such, the exact reattachment angles varied slightly between experimental runs. The hysteresis loops of C_l (cf. Fig. 12) represent individual experimental runs.

Where immediate-leading-edge stall has occurred, shifting the separation point from about $0.2c$ to $0.01c$ due to increasing α , it does not return to $0.2c$ at the same angle when α is decreased. Instead, the separation point gradually moves to about $0.09c$ before abruptly shifting back downstream at $\alpha = 19.9^\circ$, $\alpha = 26.0^\circ$ and $\alpha = 29.0^\circ$ for $Re_c = 0.5 \times 10^6$, $Re_c = 1.0 \times 10^6$ and $Re_c = 1.5 \times 10^6$, respectively. For $Re_c = 0.5 \times 10^6$, flow reattachment occurs at an angle below α_{stall} . Thus, the flow reattaches to the entire suction side at once, and no trailing-edge separation is present. For $1.0 \times 10^6 \leq Re_c \leq 1.5 \times 10^6$, the flow reattaches to the front of the suction side at an angle above α_{stall} , leaving the trailing-edge region separated. Once the separation point has shifted back downstream, the pressure distributions are identical to those at increasing α , suggesting that there is no hysteresis in the turbulent trailing-edge separation. Because

the forward shift of the separation point is associated with a drastic loss of lift, the hysteresis leads to significant differences in C_l for increasing and decreasing α (cf. Fig. 12). For $Re_c \geq 3.0 \times 10^6$, the flow does not reattach to the suction side at α_{stall} , but instead at a slightly lower angle. The width of the hysteresis loop increases slightly with Reynolds number before leveling off around $\Delta\alpha = 1.75^\circ$ at $Re_c = 5.9 \times 10^6$ (cf. Fig. 9a).

6 Discussion

6.1 Attached flow

Attached flow around an airfoil at high Re_c is expected to exhibit smaller Reynolds number effects than separated flow. However, the state of the boundary layer is expected to exhibit Reynolds number effects, which can affect the overall performance even in this regime. It is certain that the boundary layers along both the top and bottom surfaces of the airfoil transition to turbulence at some point along the chord for all Reynolds numbers, because the airfoil used here is sufficiently thick that a purely laminar boundary layer would separate even at $\alpha = 0^\circ$ (Mueller and Batill 1982). For $Re_c \leq 1.5 \times 10^6$, where transition visibly occurs via a laminar separation bubble, this bubble acts as a trip by fixing the location of the transition region near the laminar separation point. The change in the Reynolds number trends of many quantities around $Re_c = 1.5 \times 10^6$, as well as the discussion on stall in Sect. 6.2 suggest that for $Re_c \geq 2.0 \times 10^6$ the flow naturally transitions to turbulence upstream of the point where a laminar separation bubble would otherwise have formed, here referred to as the hypothetical laminar

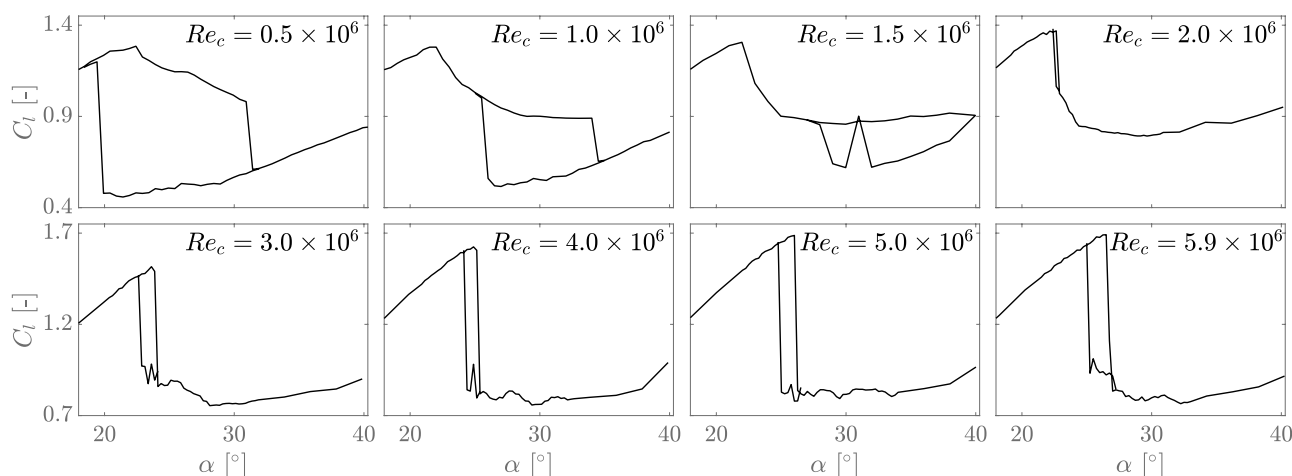


Fig. 12 Hysteresis loops in C_l due to stepwise increasing and decreasing α . In all cases, the upper curve corresponds to increasing α and the lower curve to decreasing α . Where no hysteresis occurred only the increasing path is shown for clarity

separation point. The use of transition sensors (e.g. Klein et al. 2014) in future studies could provide further clarity.

Aerodynamic theory predicts that the pressure drag coefficient C_d and the aerodynamic center $a.c.$ should not vary with Re_c . According to thin airfoil theory, the $a.c.$ of a two-dimensional symmetric airfoil is located at the quarter-chord point. However, experimental data often show slight variations in the location of the $a.c.$, and consequently a non-zero moment around the quarter-chord point (Loftin and Smith 1949). Furthermore, the three-dimensionality of the airfoil might affect the location of the $a.c.$.

The presence of a laminar separation bubble typically alters the effective shape of the airfoil, leading to a slight amount of camber which decreases with bubble size. The size of a laminar separation bubble has been shown to decrease with increasing Re_c because the location at which the free shear layer transitions to turbulence and reattaches moves upstream (Tani 1964). This might explain the decrease in C_l , C_d and the $a.c.$ over the range $0.5 \times 10^6 \leq Re_c \leq 1.5 \times 10^6$. The trends as Reynolds number is increased beyond $Re_c = 1.5 \times 10^6$ are less straightforward. Interestingly, the $a.c.$ moves toward its theoretical two-dimensional value of 0.25 at infinite Re_c , possibly because the earlier transitioning of the boundary layers and their slower growth once turbulent cause the effective airfoil shape to approach the geometric shape. In the pressure distributions, this is manifested as a slight Reynolds number trend in the magnitude of the suction peak.

6.2 Stall

Thick airfoils have previously been shown to stall gradually from the trailing edge, while thin airfoils tend to stall abruptly from the leading edge (Gault 1957; Loftin and Bursnall 1948). In the data presented here, the stall type is shown to vary with Reynolds number, depending on the relative locations of the hypothetical turbulent and laminar separation points. The gradual stall behavior for $Re_c \leq 1.5 \times 10^6$ is in agreement with existing data at comparable Reynolds numbers (Angell et al. 1990), while the sudden stall for $Re_c \geq 2.0 \times 10^6$ has not previously been observed at high Re_c . The presence of laminar separation bubbles and the gradual trailing-edge stall at the lower Re_c indicate turbulent separation. Interestingly, the laminar separation bubbles persist up to large α , at which higher Reynolds number flows have already undergone leading-edge stall. Presumably, this is because the turbulent flow separation further downstream leads to an increase in $C_{p,min}$ at the leading edge, and thus, a decrease in the adverse pressure gradient which the bubble has to withstand, allowing it to persist to higher α .

The turbulent separation point depends on Re_c . As Re_c increases, the viscous length scale of the turbulent boundary layer changes such that the velocity gradient near the

wall increases. As a result, the flow is able to withstand a higher pressure gradient before separating, so that turbulent separation is expected to occur at higher α as Re_c increases. Indeed, trailing-edge separation appears to occur only for $Re_c \leq 3.0 \times 10^6$, and the angle at which it first occurs increases with Reynolds number. For $Re_c \geq 4.0 \times 10^6$, the velocity gradient is presumably high enough that turbulent separation does not occur before the flow reaches the trailing edge for all angles below the leading-edge-stall angle (see below).

For $Re_c \geq 3.0 \times 10^6$, the transition to turbulence likely occurs naturally upstream of the point where laminar separation would have otherwise occurred. This hypothetical laminar separation point is expected to be almost invariant with Re_c and moves upstream with increasing α . If the laminar separation point moves upstream of the transition region, the previously attached flow separates at the laminar separation point, leading to abrupt stall. The angle at which stall occurs should increase with Re_c as the transition region moves upstream with increasing Re_c . However, at any given angle, the chord location of the separation point once stalled should not vary with Re_c . This is consistent with the drastic leading-edge stall observed for $Re_c \geq 2.0 \times 10^6$. A laminar separation bubble might still form temporarily as the laminar separation point moves upstream of the turbulent transition region, but likely bursts quickly due to the high pressure gradient. Naturally, α_{stall} cannot increase indefinitely. The leveling off around $Re_c \geq 7.0 \times 10^6$ might therefore indicate that the transition region no longer moves upstream with increasing Re_c due to the favourable pressure gradient near the leading edge.

The presence of leading-edge stall on an airfoil of 21% thickness, and the low C_l in the separated region stand in contrast to previous tests by Jacobs (1931a), Jacobs (1931b) and Angell et al. (1990). However, in the experimental setup used here both the freestream turbulence and the surface roughness of the airfoil were relatively low. Swalwell et al. (2001) showed that a decrease in inflow turbulence can shift the stall behavior from gradual trailing-edge stall to abrupt leading-edge stall by moving the transition region downstream. It is plausible that previous data sets were acquired at higher inflow turbulence or surface roughness which facilitated transition and thus led to turbulent trailing-edge stall.

6.3 Separated flow

Once the flow is separated on large parts of the suction side, the airfoil acts as a bluff body, and certain similarities emerge with flows over other bluff bodies such as circular cylinders. It is important to note that the separation point observed in the data does not necessarily indicate the location where separation first occurred. Rather, the initial flow

separation might lead to a readjustment of the pressure field and thus of the separation point itself. As such, the static separation point is not necessarily dependent on the pressure distribution prior to stall.

The relatively constant suction peak at all α suggests that at any Re_c there is a given pressure differential between the suction peak and the separated region which the flow can withstand. This pressure differential determines the magnitude of the suction peak independently of α and the separation point. The pressure gradient then determines the separation point for both laminar and turbulent separation. The higher surface curvature near the leading edge at high α leads to a higher adverse pressure gradient and thus causes the separation point to be located further upstream. As the angle of attack approaches $\alpha = 40^\circ$, an increase in the angle presumably has negligible effect on the surface curvature upstream of the separation point due to the large nose region of the airfoil. Thus, the separation ceases to move upstream with increasing α .

The Reynolds number trend in the location of the separation point for $Re_c \leq 2.0 \times 10^6$ indicates that the lower Reynolds number flows are able to withstand a higher overall pressure differential. This trend is counter-intuitive because a higher Re_c implies a higher velocity gradient near the surface, which should allow the flow to withstand a higher pressure differential, but instead the flow separates further upstream. Studies on airfoils and circular cylinders have shown that the presence of a laminar separation bubble can delay turbulent separation compared to a naturally transitioning flow (Jones et al. 1969; Schewe 2001). This is attributed to the increased mixing in the free shear layer, which increases the Reynolds stresses in the reattached boundary layer. It is therefore plausible that a larger separation bubble will delay stall more than a smaller one. Since the size of the laminar separation bubble decreases with increasing Re_c , this would lead to the trend observed here.

Both the shape of the separated region and its pressure field potentially vary with Re_c , as the transition region of the separated shear layer moves upstream with increasing Re_c . While the shape of the wake cannot be inferred from the surface pressure distributions, the trend in mean surface pressure $C_{p,sep}$ indicates generally better pressure recovery at lower Re_c and is reminiscent of the related base pressure trend shown by Roshko (1993) in the flow over a circular cylinder.

The significant upstream shift of the separation point at $Re_c \leq 1.5 \times 10^6$ as α is further increased towards $\alpha = 40^\circ$, here referred to as immediate-leading-edge stall, is reminiscent of laminar separation over a circular cylinder and is possibly induced by the bursting of the separation bubble. Once the bubble bursts, the flow separates at the laminar separation point. The resulting sudden increase in the size of the separated region might cause a redistribution of the

pressure field such that the separation point moves upstream to the immediate leading edge. The bubble bursts when the turbulent shear layer is unable to reattach to the surface due to an increase in curvature or adverse pressure gradient as the laminar separation point moves upstream with increasing α . The sooner the free shear layer transitions to turbulence, the more likely it is to reattach. Thus, an increase in Re_c delays the bursting of the bubble to higher α . However, it is unclear why no immediate-leading-edge stall is observed for $Re_c \geq 2.0 \times 10^6$ where separation is presumably already laminar. It is possible that in order to adopt immediate-leading-edge stall, the flow requires a significant perturbation such as that caused by the bursting of the laminar separation bubble, which is expected to happen only at low Re_c .

6.4 Hysteresis in angle of attack

Hysteresis of the flow when changing the angle of attack implies that over a particular range of α there are two stable flow configurations, and the flow condition upon entering this range determines which configuration the flow assumes. It should be noted that the limited aspect ratio of the airfoil in this study potentially affects the hysteresis. For $Re_c \leq 1.5 \times 10^6$, the upstream shift of the separation point to immediate-leading-edge stall presumably leads to a readjustment of the pressure field. Thus, the adverse pressure gradient might be higher for decreasing α than for increasing α . Furthermore, the separation point is located far upstream at around $0.01c$, and the NACA 0021 has a large rounded nose region, so that the flow upstream of the separation point does not experience a change in surface curvature until α has been decreased significantly below the angle at which the shift initially occurred.

The hysteresis at high Re_c could be an indication that the separation point observed in the equilibrated pressure distribution following stall is not the point at which the boundary layer originally separated from the surface, but that readjustments in the pressure field immediately after stall push the separation point slightly upstream. In order for the flow to reattach, the separation point might have to return to its instantaneous location at stall, which would require α to be lower in order to account for the shift in the pressure field. The presence of turbulent trailing-edge stall and the generally less abrupt stall behavior at lower Re_c might reduce or eliminate the shift in the pressure field after stall in these cases.

7 Conclusions

The results of this study suggest that the effects of Reynolds number on stall behavior and separated flow conditions are more complex than often assumed. Reynolds

number effects are expected to occur whenever turbulent boundary layers or shear layers are present. Here, they are shown to occur even when stall is ultimately laminar. The stall type is determined by the relative locations of the hypothetical laminar separation point, the transition region, and the hypothetical turbulent separation point. Aside from simply moving the transition region upstream, an increasing Reynolds number moves the hypothetical turbulent separation point downstream. By moving it all the way to the trailing edge, an increasing Reynolds number can cause the stall behavior to shift from trailing-edge stall to leading-edge stall, particularly if low surface roughness and free stream turbulence lead to a relatively high critical Reynolds number.

The separated flow behavior appears to constitute a subtle balance between the magnitude of the suction peak and the location of the separation point. The magnitude of the suction peak is relatively constant with angle of attack and decreases with Reynolds number, while the separation point moves upstream with both increasing angle of attack and Reynolds number. Separation thus seems to be determined more by the total pressure differential from suction peak to separation point than by the pressure gradient at any given point.

Hysteresis of the flow with angle of attack is shown to occur across the entire Reynolds number range, although the hysteresis found at the higher Reynolds numbers is fundamentally different from that at lower Reynolds numbers. The observed hysteresis effects have strong implications for dynamic stall modelling, as they constitute the quasi-steady limit that pitching airfoils are expected to approach at low reduced frequencies. Furthermore, the findings caution against extrapolating low Reynolds number airfoil data to high Reynolds numbers, as the observed trends with Reynolds number are not continuous. Nevertheless, the data suggest that the aerodynamics eventually approach Reynolds number invariance. For the geometry studied here, this occurred for $Re_c \geq 7.0 \times 10^6$. While the three-dimensional effects present here are not expected to significantly alter any Reynolds number trends observed, the applicability of these findings to two-dimensional airfoils needs to be investigated.

Appendix

Error analysis

The uncertainties for various measured parameters are listed in Table 2. They are based on manufacturer ratings

Table 2 Total uncertainties for various measured quantities in the experimental study. The values for the pitot-static pressure transducer, density, and viscosity were taken from Miller et al. (2018), where the same sensing equipment was used

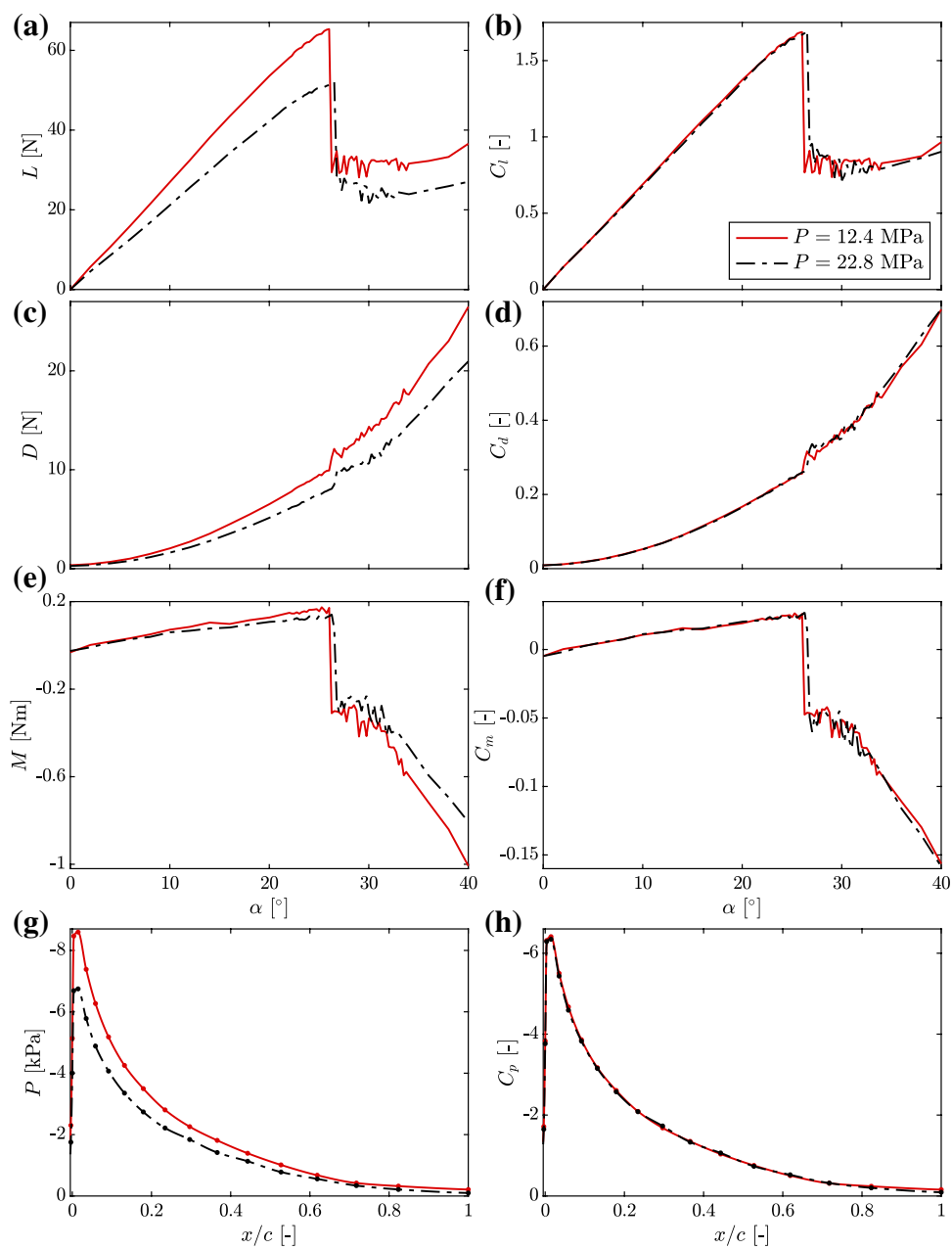
Quantity	Variable	Total uncertainty
Airfoil surface pressure (10 kPa, 6.9 kPa, 2.5 kPa ranges)	p	$\pm 25, \pm 17.24, \pm 6.22$ [Pa]
Angle of attack	α	± 0.105 [°]
Pitot-static pressure transducer	\bar{p}	± 34.47 [Pa]
Density	ρ	± 0.36 [%]
Viscosity	μ	± 0.8 [%]

Table 3 Uncertainties in final quantities were propagated from manufacturer ratings. The error at $Re_c = 5.0 \times 10^6$ is the mean difference between the two data sets used in Fig. 13

Quantity	Variable	Propagated uncertainty	Measured error at $Re_c = 5.0 \times 10^6$
Reynolds number	Re	$\pm 0.97\%$	0.55%
Lift coefficient	C_l	± 0.063	0.034
Drag coefficient	C_d	± 0.056	0.009
Moment coefficient	C_m	± 0.33	0.001
Aerodynamic center	$a.c.$	± 0.26	0.001

and include linearity, hysteresis, and temperature influences combined in a root-mean-square value for each sensor. These errors were propagated to determine the uncertainties in the final quantities reported in this paper. These uncertainties are given in Table 3. However, because the instrumentation was re-zeroed before every test to account for any systematic offsets, the actual uncertainties were lower. Figure 13 shows two experiments conducted at the same Re_c , but at different pressure-velocity combinations. While the dimensional quantities vary as a result of the differing operating conditions, the non-dimensional quantities collapse well, indicating both repeatability and high accuracy of the data. In particular, the collapse of the moment coefficient is noteworthy because its propagated error is on the order of the measurement itself. It suggests that the actual accuracy is significantly higher than the propagated errors in Table 3 suggest. However, the uncertainty increases slightly with decreasing Re_c due to decreasing pressure sensor loading, so that the errors in the measurements at the lowest Re_c are likely larger than in the case of $Re_c = 5.0 \times 10^6$ shown here. The stall angles varied between experimental runs. This is not due

Fig. 13 Dimensional (left) and non-dimensional (right) values from two experiments at $Re_c = 5.0 \times 10^6$ at different static pressures and velocities. The excellent collapse of the plots on the right indicates high accuracy of the pressure sensors



to experimental error, but to stochastic variability of the flow itself.

Acknowledgements The authors would like to thank Dan Hoffman at the Princeton Gas Dynamics Laboratory for his great help and advice in setting up the experiment, as well as Jason Liu for conducting surface roughness measurements.

Author Contributions C.E.B. and J.K. carried out the experiments. C.E.B. and J.K. analyzed the data. C.E.B. wrote the manuscript. J.K. designed the experiment and built the setup. All authors reviewed the paper. M.O.L.H. and M.H. provided scientific advice and contributed to study supervision.

Funding The authors gratefully acknowledge the support of the National Science Foundation under grant CBET 1652583, the United States Department of Defense through the National Defense Science and Engineering Graduate Fellowship, and the Otto Mønsteds Foundation through a travel grant.

Availability of data The data from this study are publicly available at <https://doi.org/10.34770/9mv0-zd78>.

Declarations

Conflict of interest The authors declare that they have no conflict of interest.

References

Angell R, Musgrove P, Galbraith RM, Green R (1990) Summary of the collected data for tests on the NACA 0015, NACA 0018, NACA 0021, NACA 0025 and NACA 0030 aerofoils. Tech. Rep. Aero Rpt 9005, Glasgow University

FloWind (1996) Final project report : High energy rotor development, test and evaluation. Tech. Rep. SAND96-225, Sandia National Laboratories

Fox TA, West GS (1990) On the use of end plates with circular cylinders. *Exp Fluids* 9(4):237–239

Gault D (1957) A correlation of low-speed, airfoil-section stalling characteristics with Reynolds number and airfoil geometry. Tech. Rep. NACA-TN-3963, National Advisory Committee for Aeronautics

Hefer G (2003) Etw - a facility for high Reynolds number testing. In: Sobieczky H (ed) IUTAM Symposium Transsonicum IV. Fluid Mechanics and its Applications, Springer, Dordrecht, vol 73, pp 157–164

Hoerner S (1975) Fluid Dynamic Lift. Hoerner Fluid Dynamics, Brick Town

Holmes BJ, Obara CJ, Martin GL, Domack CS (1986) Manufacturing tolerances for natural laminar flow airframe surfaces. *SAE Trans* 850863:522–529

Jacobs E (1931a) The aerodynamic characteristics of eight very thick airfoils from tests in the variable density wind tunnel. Tech. Rep. NACA-TR-391, National Advisory Committee for Aeronautics

Jacobs E (1931b) Tests of six symmetrical airfoils in the variable density wind tunnel. Tech. Rep. NACA-TN-385, National Advisory Committee for Aeronautics

Jacobs E, Anderson R (1931) Large-scale aerodynamic characteristics of airfoils as tested in the variable density wind tunnel. Tech. Rep. NACA-TR-352, National Advisory Committee for Aeronautics

Jacobs E, Sherman A (1937) Airfoil section characteristics as affected by variations of the Reynolds number. Tech. Rep. NACA-TR-586, National Advisory Committee for Aeronautics

Jiménez J (2007) High Reynolds number flows about bodies of revolution with application to submarines and torpedoes. PhD thesis, Princeton University

Jiménez J, Hultmark M, Smits A (2010) The intermediate wake of a body of revolution at high Reynolds numbers. *J Fluid Mech* 659:516–539

Jones G, Cincotta J, Walker R (1969) Aerodynamic forces on a stationary and oscillating circular cylinder at high Reynolds numbers. Tech. Rep. NASA-TR-R-300, National Aeronautics and Space Administration

Klein C, Henne U, Sachs W, Beifuss U, Ondrus V, Bruse M, Lesjak R, Löhr M (2014) Application of carbon nanotubes (CNT) and temperature-sensitive paint (tsp) for the detection of boundary layer transition. 52nd AIAA Aerospace Sciences Meeting AIAA 2014-1482

Loftin L, Bursnall W (1948) The effects of variations in Reynolds number between 3.0×10^6 and 25.0×10^6 upon the aerodynamic characteristics of a number of NACA 6-series airfoil sections. Tech. Rep. NACA-TN-1773, National Advisory Committee for Aeronautics

Loftin L, Smith H (1949) Aerodynamic characteristics of 15 NACA airfoil sections at seven Reynolds numbers from 0.7×10^6 to 9.0×10^6 . Tech. Rep. NACA-TN-1945, National Advisory Committee for Aeronautics

McCullough G, Gault D (1951) Examples of three representative types of airfoil-section stall at low speed. Tech. Rep. NACA-TN-2502, National Advisory Committee for Aeronautics

Miller M, Duvvuri S, Brownstein I, Lee M, Dabiri J, Hultmark M (2018) Vertical-axis wind turbine experiments at full dynamic similarity. *J Fluid Mech* 844:707–720

Mueller T, Batill S (1982) Experimental studies of separation on a two-dimensional airfoil at low Reynolds numbers. *AIAA J* 20(4):457–463

Raciti Castelli M, Englano A, Benini E (2011) The Darrieus wind turbine: Proposal for a new performance prediction model based on CFD. *Energy* 36(8):4919–4934

Roshko A (1993) Perspectives on bluff body aerodynamics. *J Wind Eng Ind Aerodyn* 49:79–100

Schewe G (2001) Reynolds-number effects in flow around more-or-less bluff bodies. *J Wind Eng Ind Aerodyn* 89(14–15):1267–1289

Swalwell K, Sheridan J, Melbourne W (2001) The effect of turbulence intensity on stall of the NACA 0021 aerofoil. 14th Australasian Fluid Mechanics Conference pp 941–944

Szepessy S, Bearman PW (1992) Aspect ratio and end plate effects on vortex shedding from a circular cylinder. *J Fluid Mech* 234:191–217

Tani I (1964) Low-speed flows involving bubble separations. *Prog Aerosp Sci* 5:70–103

Von Doenhoff A, Abbott FJ (1947) The Langley two-dimensional low-turbulence pressure tunnel. Tech. Rep. NACA-TN-1283, National Advisory Committee for Aeronautics

Wahls R (2001) The national transonic facility: A research retrospective. 39th AIAA Aerospace Sciences Meeting and Exhibit AIAA-2001-0754

Zagarola M (1996) Mean-flow scaling in turbulent pipe flow. PhD thesis, Princeton University

Publisher's Note Springer Nature remains neutral with regard to jurisdictional claims in published maps and institutional affiliations.